

A Wide Range of CO : H₂ Syngas Proportions Enabled by Tellurization-Induced Amorphous Telluride-Palladium Surface

Kailei Cao^{a,d}, Yujin Ji^{b,d}, Shuxing Bai^a, Xiaoqing Huang^{a,c,*}, Youyong Li^b and Qi Shao^{a,*}

a. College of Chemistry, Chemical Engineering and Materials Science, Soochow University, Jiangsu 215123, China.

b. Institute of Functional Nano & Soft Materials (FUNSOM), Soochow University, Jiangsu, 215123, China.

c. State Key Laboratory of Physical Chemistry of Solid Surfaces, College of Chemistry and Chemical Engineering, Xiamen University, Xiamen, 361005, China.

d. K.C and Y.J. are equally contributed.

Experimental Procedures

1.1 Chemicals.

Palladium (II) acetylacetonate ($\text{Pd}(\text{acac})_2$, 98%) and polyvinylpyrrolidone (PVP, MW = 58000) were purchased from J&K Scientific Ltd. Telluric acid ($\text{Te}(\text{OH})_6$, 97%) was purchased from Aladdin. N,N-dimethylformamide (DMF) and potassium bicarbonate (KHCO_3) were purchased from Sinopharm Chemical Reagent Co. Ltd. (Shanghai, China). High purity CO_2 (>99.9%) and Ar (>99.9%) were purchased from Wugang, Shanghai. The water (18 $\text{M}\Omega/\text{cm}$) used in all experiments was prepared by passing through an ultra-pure purification system. All chemicals and solvents used in this work were used as received without further purification.

1.2 Synthesis of Pd NPs.

In a typical preparation of Pd NPs, $\text{Pd}(\text{acac})_2$ (10 mg), PVP (32 mg) and DMF (10 mL) were added into a vial (volume: 35 mL). After the vial had been capped, the mixture was ultrasonicated for 5 min. After that, the resulting homogeneous mixture was transferred into a 20 mL Teflon-lined autoclave and subsequently heated from room temperature to 150 °C in 0.5 h and maintained at 150 °C for 8 h, before it cooled to room temperature. The resulting colloidal products were collected by centrifugation and washed with an ethanol/acetone mixture.

1.3 Synthesis of Te-Pd NPs.

In a typical preparation of 8% Te-Pd NPs, 0.63 mg telluric acid was added to the above Teflon-lined autoclave that contains Pd NPs-DMF solution and stirred for 20 min at room temperature. After that, the resulting homogeneous mixture heated from room temperature to 150 °C in 0.5 h and maintained at 150 °C for 2 h, before it cooled to room temperature. The resulting colloidal products were collected by centrifugation and washed with an ethanol/acetone mixture. The synthetic conditions for 1.4% Te-Pd NPs, 4.5% Te-Pd NPs and 16% Te-Pd NPs are similar with that of 8% Te-Pd NPs synthesis except for adding 0.19, 0.38 and 1.26 mg telluric acid, respectively.

1.4 Preparations of supported catalysts.

8 mg C powder (VC-X72) and 3 mL ethanol were added into a vial (volume: 35 mL) and then ultrasonicated for around 0.5 h. After that, 15 mL chloroform was added into the vial. Simultaneously, the Pd NPs or Te-Pd NPs dispersed ethanol solution was also prepared. The above two solutions were then mixed and stirred at 1000 rpm for 2 h. The products were separated by centrifugation and washed

with acetone, and then dried at room temperature in a oven. Before CO₂RR test, catalysts were subjected to anneal in air for 1 hour at 200 °C, which were named as Pd NPs/C or Te-Pd NPs/C.

1.5 Cathode preparation.

Typically, 1.5 mg catalyst and 10 μL Nafion solution (5 wt%) were dispersed in 300 μL isopropyl alcohol by sonicating for 0.5 h to form a homogeneous ink. 20 μL homogeneous ink was then loaded onto a glassy carbon electrode (GCE) with the geometric surface area of 0.196 cm² and dried under ambient conditions.

1.6 Electrochemical measurements.

The CO₂ electroreduction experiments were carried out in a gas-tight two-chamber electrochemical cell with a Nafion-117 proton exchange membrane (PEM) as the separator. The Nafion 211 membrane was pretreated with 5% H₂O₂ solution and 10% H₂SO₄ for 1 h at 80 °C, respectively, and deionized water for another 1 h. The electrochemical experiments were conducted on CHI660E electrochemical analyzer (CHI Instruments) by using a three-electrode configuration (synthetic catalysts as the working electrode, the carbon rod as the counter electrode, and Ag/AgCl as the reference electrode). All potentials were converted to reversible hydrogen electrode (RHE). All provided current density values were normalized to the geometric surface area. For electrochemical CO₂RR, *i*-*t* measurement was performed at a fixed potential for 1 h with maintaining a constant CO₂ flow rate (30 sccm) in the CO₂-saturated 0.1 M KHCO₃ electrolyte. CO₂ gas was bubbled for 30 min before the measurement. Linear sweep voltammetry curves were collected in CO₂-saturated (or Ar-saturated) 0.1 M KHCO₃ solution with the scan rate of 10 mV s⁻¹. The outlet gases of cathodic chamber were analyzed by gas chromatography (GC, Aligent 7890B) equipped with a molecular sieve 5 A and two porapak Q columns. Ar was used as the carrier gas. Gas products were first analyzed by a thermal conductivity detector (TCD), and then analyzed by flame ionization detector (FID). The concentrations of gaseous products were quantified by the integral area ratio of the reduction products to standards. The liquid products were quantified by ¹H-NMR (Aligent DD2-600) spectrometer. Typically, 1 mL electrolyte was mixed with 0.2 mL D₂O, and 0.1 mL dimethyl sulfoxide (DMSO) solution containing 1000 ppm (volume fraction). DMSO was added as an internal standard. The one-dimensional ¹H spectrum was measured with water suppression using a pre-saturation method. The FE of a product was calculated as follows:

$$FE = eF \times n/Q$$

where *e* is the number of electrons transferred of the product, *Q* is the total charge in CO₂RR process, *n* is the number of moles of the product and *F* is the Faraday constant.

1.7 Characterizations.

X-ray diffraction (XRD) was carried out on X'Pert-Pro MPD diffractometer (Netherlands PANalytical) with a Cu K α X-ray source ($\lambda = 1.540598 \text{ \AA}$). The morphology of the nanocrystals was determined by transmission electron microscopy (TEM) at an acceleration voltage of 120 kV (HITACHI HT7700). The high resolution transmission electron microscopy (HRTEM), high angle annular dark field scanning TEM (HAADF-STEM) and the corresponding EDS-mapping were conducted on a FEI Tecnai F20 transmission electron microscope at an acceleration voltage of 200 kV. Energy dispersive X-ray spectroscopy (EDS) was taken with a HITACHI S-4700 cold field-emission scanning electron microscope operated at an acceleration voltage of 15 kV. X-ray photoelectron spectra (XPS) was collected with an SSI S-Probe XPS Spectrometer. The carbon peak at 284.6 eV was used as the reference to correct for charging effects. ^1H nuclear magnetic resonance (NMR, Agilent 600 MHz) was carried out to qualitatively and quantitatively detect liquid products. The Pd loading amounts of Pd-based catalysts were determined by the inductively coupled plasma atomic emission spectroscopy (ICP-AES) (710-ES, Varian).

1.8 TPD measurements.

For CO₂-TPD measurement, 80 mg catalyst was placed at the bottom of the U-shaped quartz tube and pretreated in He flow (50 mL min⁻¹) at 200 °C for 1 h and then cooled down to 50 °C. After that, the feeding CO₂ flowed (50 mL min⁻¹) through the catalyst bed at 50 °C for 0.5 h. Then, He flow (50 mL min⁻¹) was used to remove the physisorption of CO₂ at 50 °C for 45 min. Finally, the catalyst bed was heated from 50 to 500 °C with a heating rate of 10 °C min⁻¹. A wide range of desorbing species was monitored by a thermal conductivity detector (TCD, Micromeritics AutoChem II 2920) to identify the main products generated from reactions of CO₂ on catalyst. CO-TPD measurement is similar with CO₂-TPD measurement except for replacing the CO₂ with CO/Ar (CO/Ar = 5%/95%).

1.9 Computational details and models.

Theoretical simulation part was implemented in the Vienna ab-initio software package (VASP) within the framework of spin-polarized density functional theory whose exchange-correlation functional adopted the revised PBE formula due to its better description for surface adsorption.¹⁻² The cut-off electronic energy in plane-wave basis sets was set to 400 eV and the convergence values of total energy and forces were corresponding to 10⁻⁴ eV and 0.05 eV \AA^{-1} , respectively. A 3 \times 3 \times 1 Gamma-centered Monkhost-Pack K-points meshes was sampled in the reciprocal space. In order to construct the amorphous configuration of Te-Pd NPs, we firstly constructed amorphous Te-Pd by cleaving the (001) surface slab model from crystal Te₄Pd₉. As for the kinetic barrier of the electrochemical hydrogenation step, the

potential-dependent activation energy was evaluated by the method proposed by M. J. Janik et. al. and the detailed atomic configurations for the initial, referenced, transition and final states on Te-Pd were given in Figure SX.

Supporting Figures

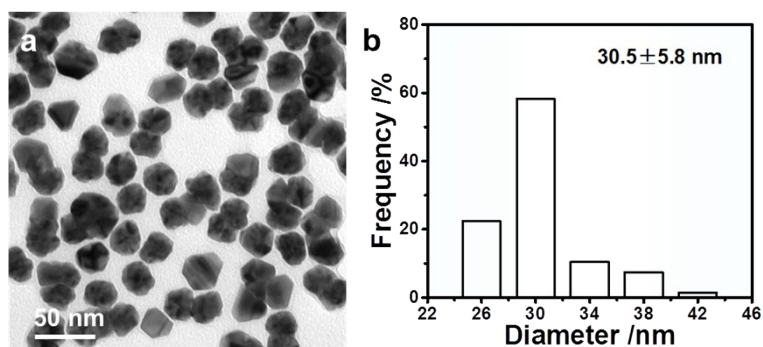


Figure S1. (a) TEM image and (b) size distribution of Pd NPs.

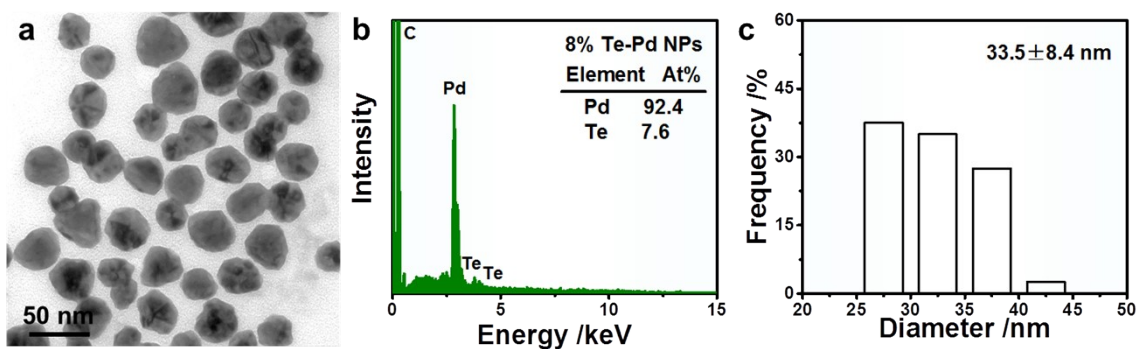


Figure S2. (a) TEM image, (b) SEM-EDS spectrum and (c) size distribution of 8% Te-Pd NPs.

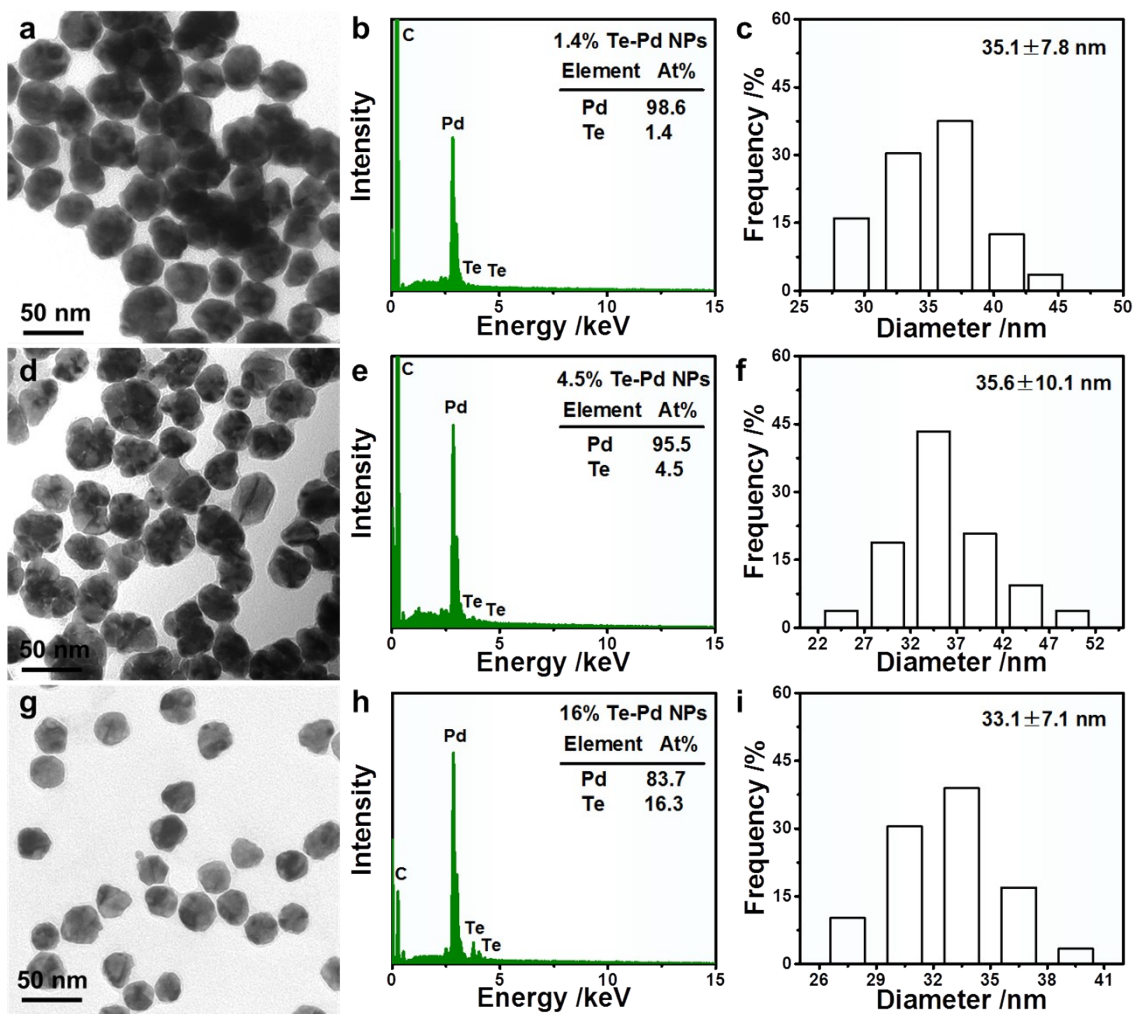


Figure S3. (a, d, g) TEM images, (b, e, h) SEM-EDS spectra and (c, f, i) size distribution of 1.4% Te-Pd NPs, 4.5% Te-Pd NPs and 16% Te-Pd NPs, respectively.

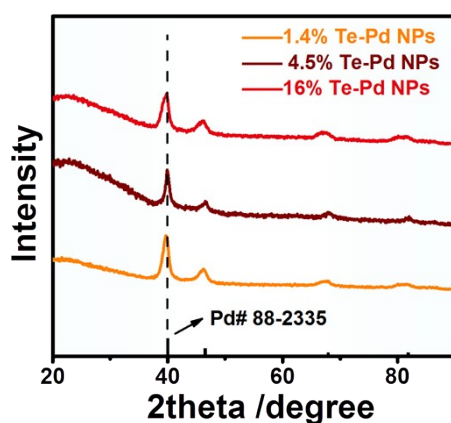


Figure S4. XRD patterns of different Te-Pd NPs.

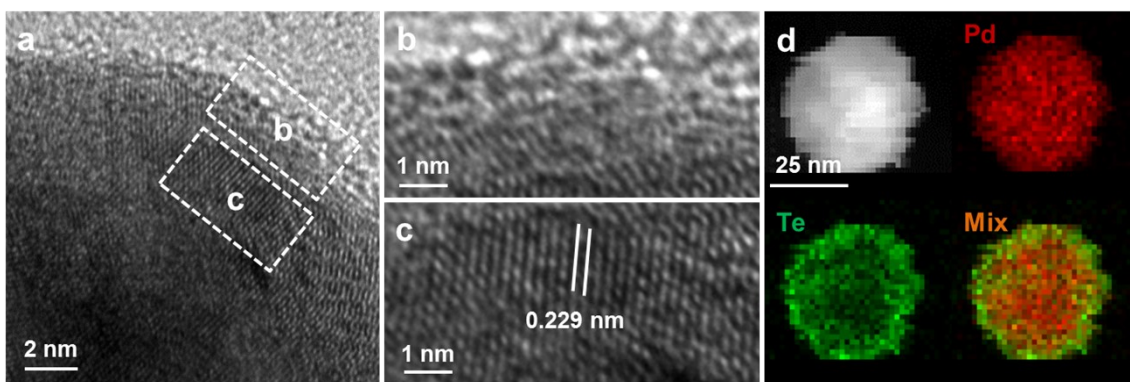


Figure S5. (a-c) HRTEM images and (d) HAADF-STEM image and EDS-mapping of 16% Te-Pd NPs.

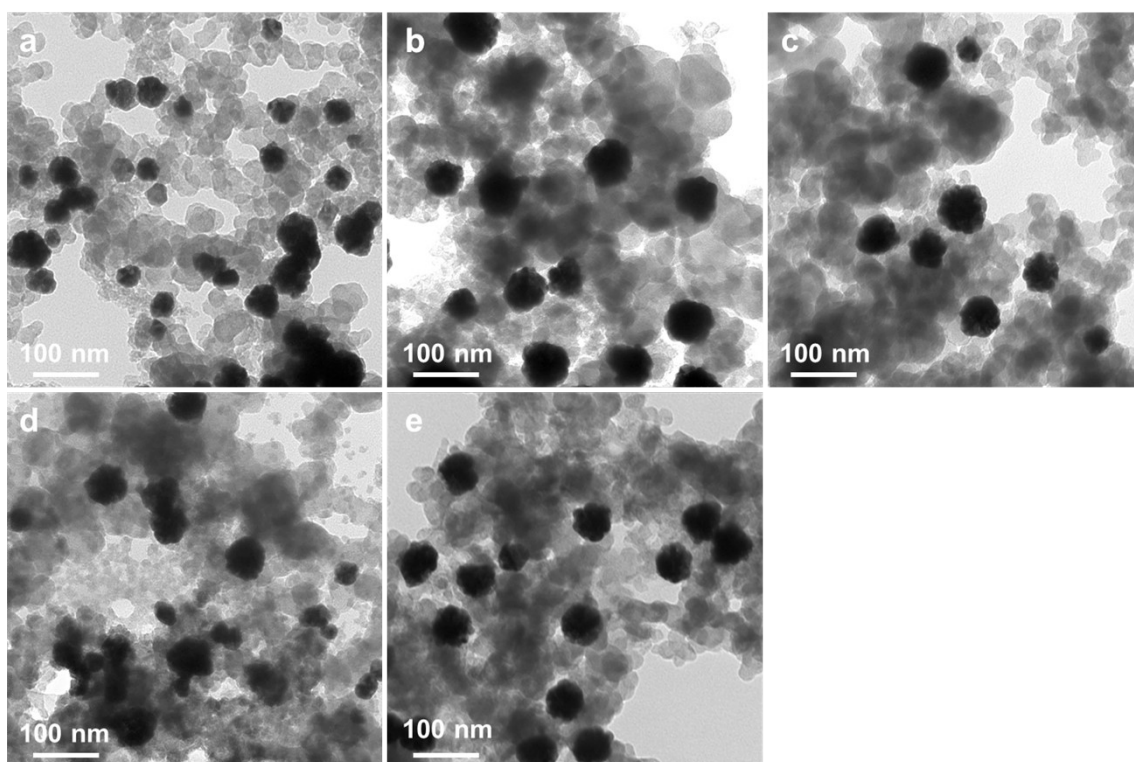


Figure S6. TEM images of (a) Pd NPs/C, (b) 1.4% Te-Pd NPs/C, (c) 4.5% Te-Pd NPs/C, (d) 8% Te-Pd NPs/C and (e) 16% Te-Pd NPs/C.

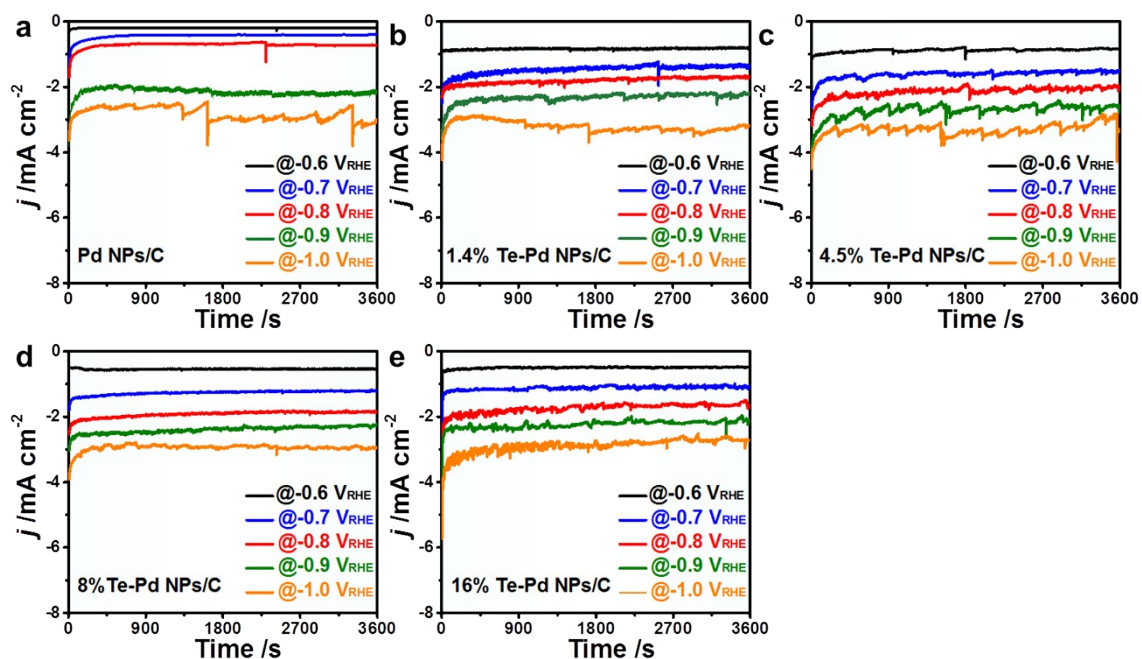


Figure S7. I-t curves for (a) Pd NPs/C, (b) 1.4% Te-Pd NPs/C, (c) 4.5% Te-Pd NPs/C, (d) 8% Te-Pd NPs/C and (e) 16% Te-Pd NPs/C.

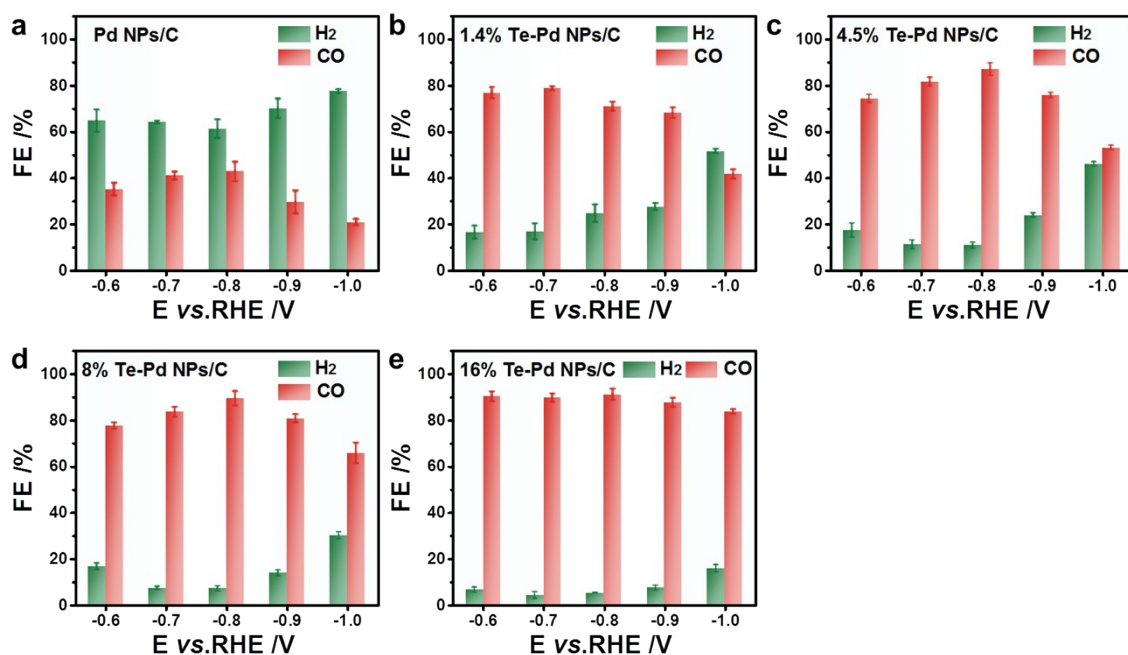


Figure S8. Faradaic efficiencies of CO₂RR products for (a) Pd NPs/C, (b) 1.4% Te-Pd NPs/C, (c) 4.5% Te-Pd NPs/C, (d) 8% Te-Pd NPs/C and (e) 16% Te-Pd NPs/C.

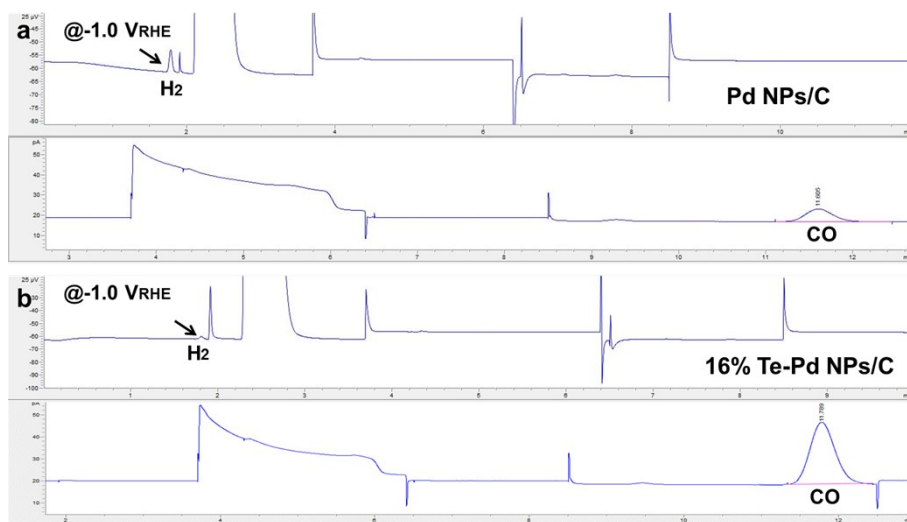


Figure S9. Gas chromatography (GC) traces of gaseous products during the electrochemical CO_2 reduction process at $-1.0 V_{\text{RHE}}$ for (a) Pd NPs/C and (b) 16% Te-Pd NPs/C.

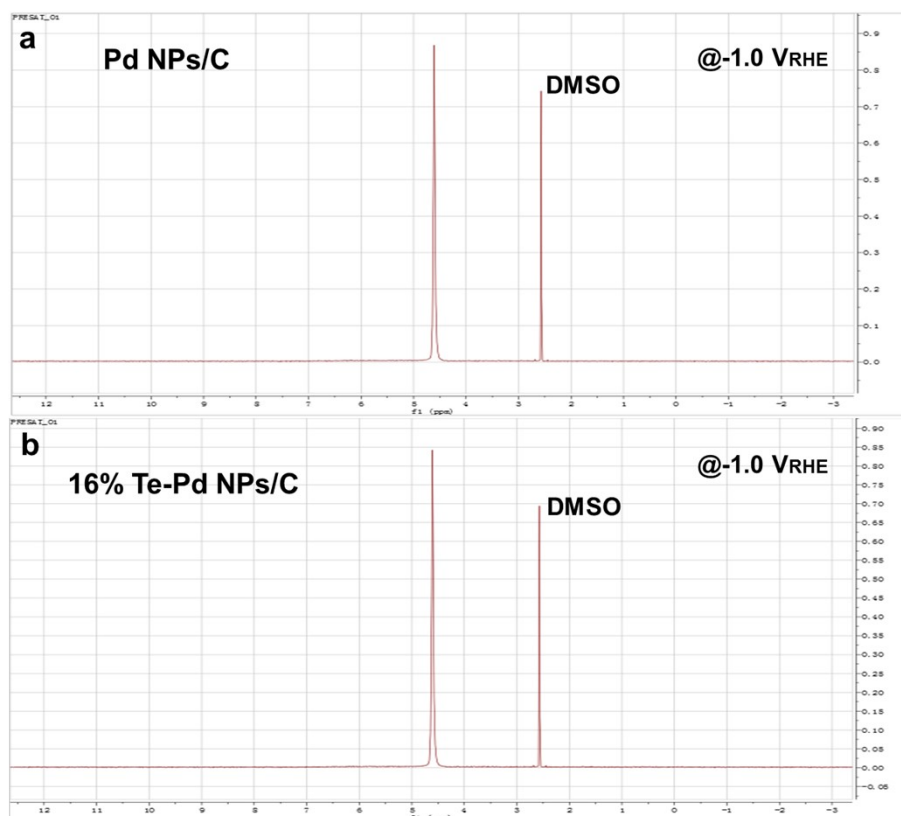


Figure S10. ^1H nuclear magnetic resonance (^1H -NMR) spectrum of the electrolyte after electrochemical CO_2 reduction at $-1.0 V_{\text{RHE}}$ for (a) Pd NPs/C and (b) 16% Te-Pd NPs/C.

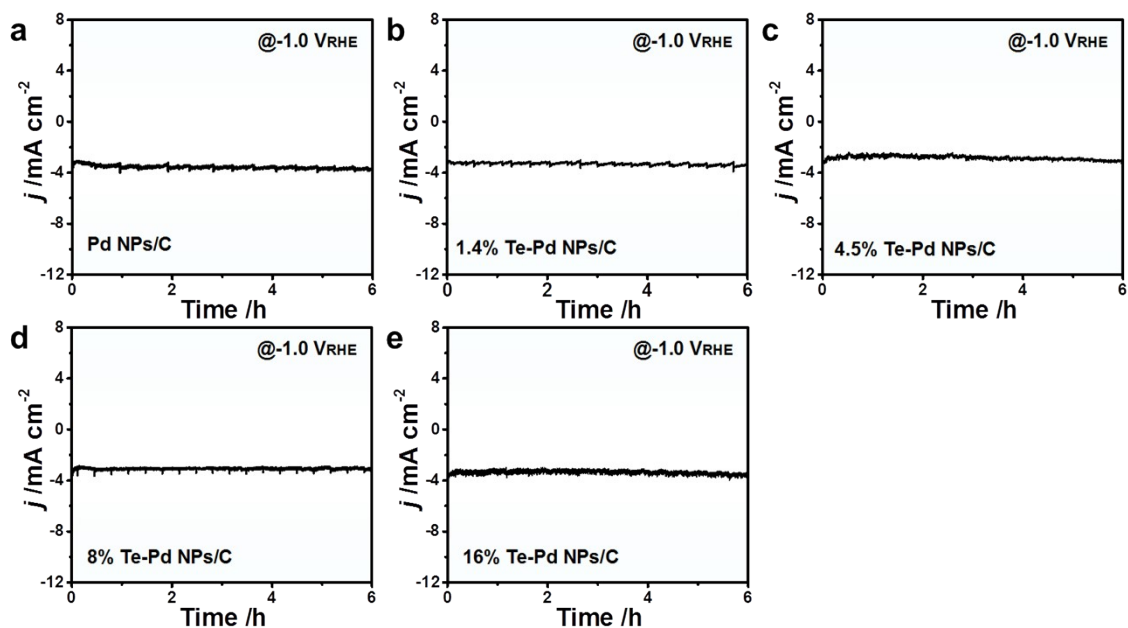


Figure S11. I-t curves at $-1.0 V_{RHE}$ of (a) Pd NPs/C, (b) 1.4% Te-Pd NPs/C, (c) 4.5% Te-Pd NPs/C, (d) 8% Te-Pd NPs/C and (e) 16% Te-Pd NPs/C during 6 h stability test.

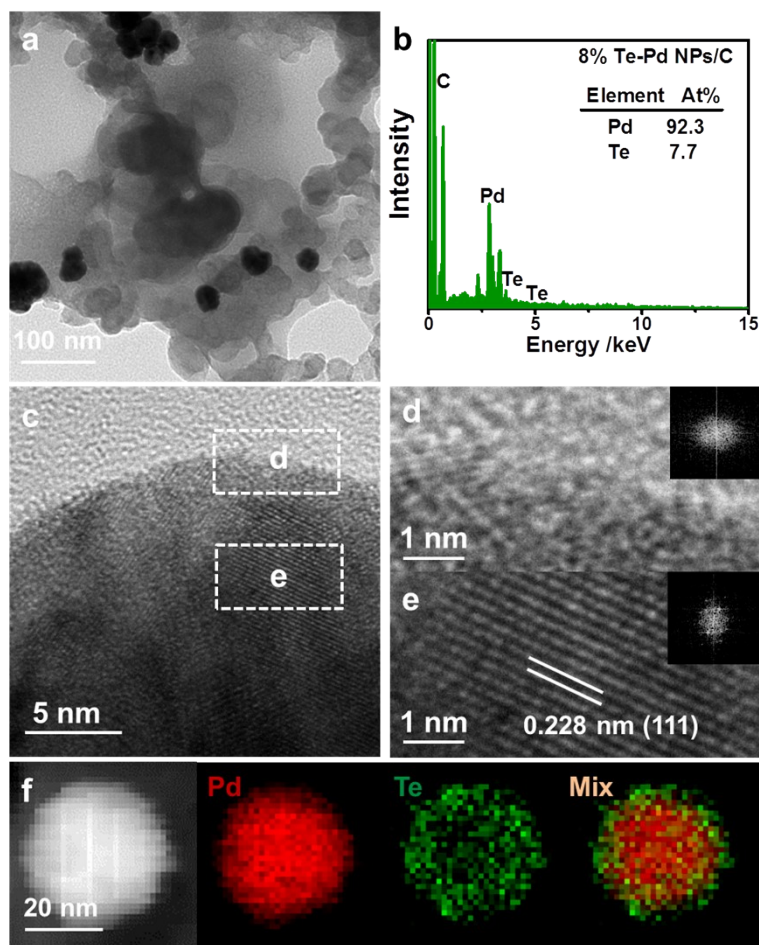


Figure S12. (a) TEM image, (b) SEM-EDS spectrum, (c-e) HRTEM image, inset in (d) and (e) is corresponded FFT images and (f) EDS-mapping of 8% Te-Pd NPs/C after 6 h stability test.

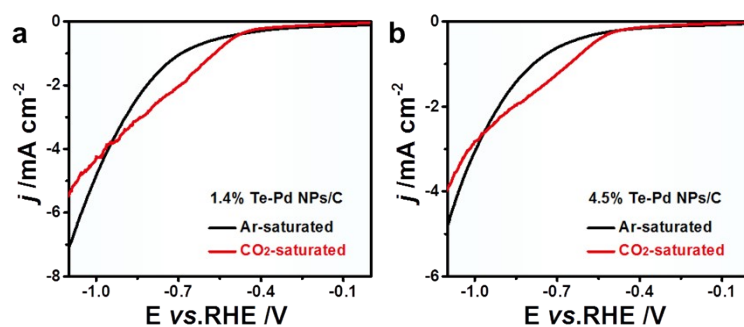


Figure S13. Linear sweep voltammetry (LSV) curves of (a) 1.4% Te-Pd NPs/C and (b) 4.5% Te-Pd NPs/C in Ar and CO₂ saturated 0.1 M KHCO₃.

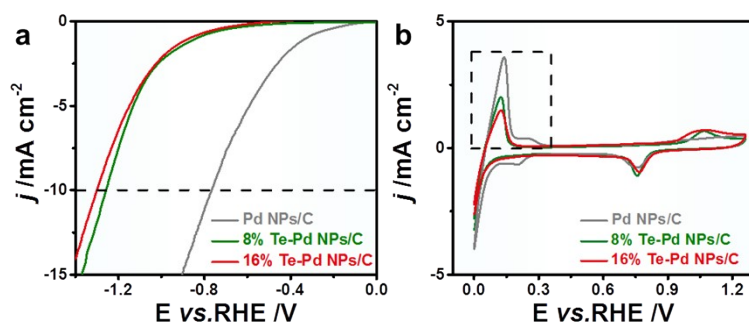


Figure S14. (a) LSV curves of Pd NPs/C, 8% Te-Pd NPs and 16% Te-Pd NPs/C in N₂ saturated 0.1 M KHCO₃ with the scan rate of 10 mV s⁻¹. (b) Cyclic voltammograms of Pd NPs/C, 8% Te-Pd NPs and 16% Te-Pd NPs/C in 0.1 M HClO₄ solution with a scan rate of 20 mV s⁻¹.

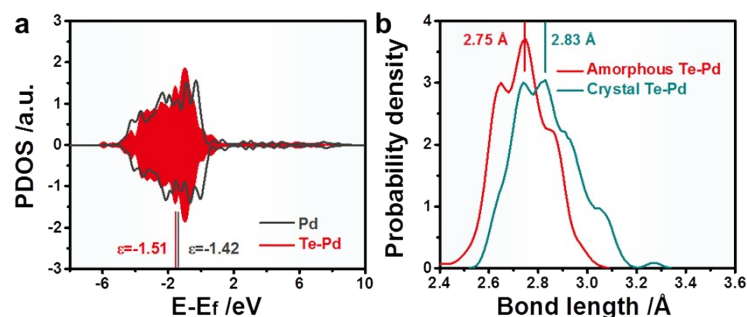


Figure S15. (a) Projected density of states of Pd *d*-orbitals in Pd NPs and Te-Pd NPs by DFT calculations. (b) Comparison of the bond length distribution among Pd atoms in crystal Te-Pd and amorphous Te-Pd NPs.

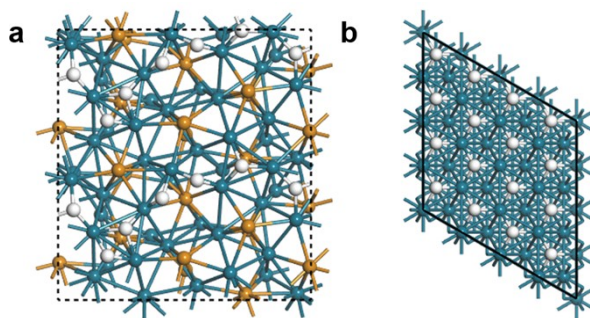


Figure S16. Surface structures of (a) Te-Pd NPs and (b) Pd NPs for the reduction of carbon dioxide at the electrode potential of $-1.0 V_{\text{RHE}}$.

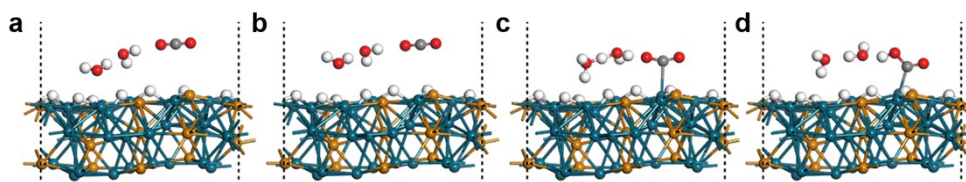


Figure S17. Side view of the (a) reference, (b) reactant, (c) transition and (d) product state of the electroreduction of CO_2 to COOH^* ($^* + \text{CO}_2 + (\text{H}^+ + \text{e}^-) \rightarrow \text{COOH}^*$).

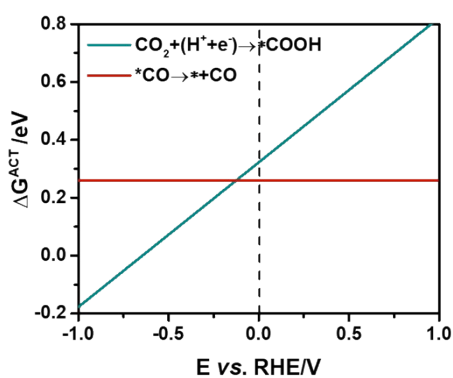


Figure S18. Comparisons of kinetic energy barriers for the electrochemical hydrogenation of CO_2 and the CO^* desorption.

Supporting Tables

Table S1. Physicochemical properties of different catalysts

Catalyst	Pd wt%
Pd NPs/C	21.3
1.4% Te-Pd NPs/C	19.8
4.5% Te-Pd NPs/C	24.4
8% Te-Pd NPs/C	24.1
16% Te-Pd NPs/C	20.5

Table S2. Comparison of CO₂RR performance of Pd NPs/C and varied Te-Pd NPs/C to those of other reported syngas electrosynthesis electrocatalysts.

Catalyst	Range of CO/H ₂ ratios	E (V vs. RHE)	Reference
Pd NPs/C x% Te-Pd NPs/C (x = 1.4, 4.5, 8, 16)	0.27~5.37	-1.0	This Work
PdM (M = Ag, Ni, Co, Cu, Pt)	0.21~2.76	-0.9	<i>Nat. Commun.</i> , 2019, 10 ,3724
Pd/C	0.25~0.76	-0.5~-1.0	<i>Energy Environ. Sci.</i> , 2017, 10 , 1180-1185
Pd NWs, Pd _{2.1} Au NWs, Pd _{0.8} Au NWs	8.53~29.9	-0.8	<i>Adv. Energy Mater.</i> , 2018, 8 , 1802238
Pd/C, Pd/NbN, Pd/VN	0.16~0.74	-0.5~-0.9	<i>Angew. Chem. Int. Ed.</i> , 2020, 202003625
4 nm AgP ₂ NCs	0.33~4.62	-0.4~-1.0	<i>Nat. Commun.</i> , 2019, 10 , 5724
CoNi-NC-x (x = 0.2, 0.5, 1, 2, 5)	0.39-3.01	-0.9	<i>Angew. Chem. Int. Ed.</i> , 2020, 59 , 3033- 3037
CdS _x Se _{1-x}	0.25~4.5	-1.2	<i>Adv. Mater.</i> , 2018, 30 , 1705872
r-Cu _{ox} (350)	1.02~3.05	-0.65~-0.65	<i>J. Mater. Chem. A</i> , 2019, 7 , 7675-7682

Table S3. Summary of Pd 3d XPS results.

Catalyst	Pd 3d _{5/2} Binding energy /eV		Pd 3d _{3/2} Binding energy /eV	
	Pd ⁰	Pd ²⁺	Pd ⁰	Pd ²⁺
Pd NPs/C	335.6	337.1	340.9	342.2
8% Te-Pd NPs/C	335.8	337.3	341.1	342.6
16% Te-Pd NPs/C	335.9	337.4	341.1	342.6

Table S4 Summary of Te 3d XPS results.

Catalyst	Te 3d _{5/2} Binding energy /eV		Te 3d _{3/2} Binding energy /eV	
	Te ⁰	Te ⁿ⁺	Te ⁰	Te ⁿ⁺
8% Te-Pd NPs/C	573.9	576.5	584.3	586.9
16% Te-Pd NPs/C	573.9	577.0	584.4	587.3

Reference

1. G. Kresse and J. Furthuller, *Phys. Rev. B*, 1996, **54**, 11169-11186.
2. B. Hammer, L. B. Hansen and J. K. Nørskov, *Phys. Rev. B*, 1999, **59**, 7413-7421.